Research

A SCIENCE PARTNER JOURNAL

Research Article

The Jahn-Teller Effect for Amorphization of Molybdenum Trioxide towards High-Performance Fiber Supercapacitor

Chenyang Yu,[1] Hai Xu,[1] Yujiao Gong,[1] Ruyi Chen,[1] Zengyu Hui,[1] Xi Zhao,[1] Yue Sun,[1] Qiang Chen,[2] Jinyuan Zhou,[3] Wenxin Ji,[4] Gengzhi Sun ⬤,[1,5] and Wei Huang ⬤[1,5]

[1]Institute of Advanced Materials (IAM), Nanjing Tech University (NanjingTech), Nanjing 211816, China
[2]School of Materials Science and Engineering, Henan Polytechnic University, Jiaozuo 454003, China
[3]School of Physical Science and Technology, Lanzhou University, Lanzhou 730000, China
[4]State Key Laboratory of High-Efficiency Coal Utilization and Green Chemical Engineering, Ningxia University, Yinchuan 750021, China
[5]Institute of Flexible Electronics (IFE), Northwestern Polytechnical University (NPU), Xi'an 710072, China

Correspondence should be addressed to Gengzhi Sun; iamgzsun@njtech.edu.cn and Wei Huang; iamwhuang@nwpu.edu.cn

Amorphous pseudocapacitive nanomaterials are highly desired in energy storage applications for their disordered crystal structures, fast electrochemical dynamics, and outstanding cyclic stability, yet hardly achievable using the state-of-the-art synthetic strategies. Herein, for the first time, high capacitive fiber electrodes embedded with nanosized amorphous molybdenum trioxide (A-MoO$_{3-x}$) featuring an average particle diameter of ~20 nm and rich oxygen vacancies are obtained via a top-down method using α-MoO$_3$ bulk belts as the precursors. The Jahn-Teller distortion in MoO$_6$ octahedra due to the doubly degenerate ground state of Mo^{5+}, which can be continuously strengthened by oxygen vacancies, triggers the phase transformation of α-MoO$_3$ bulk belts (up to 30 μm long and 500 nm wide). The optimized fibrous electrode exhibits among the highest volumetric performance with a specific capacitance (C_V) of 921.5 F cm^{-3} under 0.3 A cm^{-3}, endowing the fiber-based weaveable supercapacitor superior C_V and E_V (energy density) of 107.0 F cm^{-3} and 9.5 mWh cm^{-3}, respectively, together with excellent cyclic stability, mechanical robustness, and rate capability. This work demonstrates a promising strategy for synthesizing nanosized amorphous materials in a scalable, cost-effective, and controllable manner.

1. Introduction

Wearable devices, ranging from epidermal electronic skins [1, 2], bendable displays [3, 4], weaveable memories [5], smart textiles [6–8], and healthcare sensors [9, 10] to flexible solar cells [11, 12] and nanogenerators [13, 14], are leading a new electronic revolution and desperately demand for matchable energy storage devices with superior volumetric capacitance that can store and supply power efficiently. Among all candidates, fiber supercapacitors (FSCs) are of particular interest owing to their good flexibility, lightweight, high wearing safety, and long servicing lifespan [15–18]. Many efforts have been paid to enhance the energy performance of FSCs by incorporating pseudocapacitive nanomaterials, such as vanadium oxide (V$_2$O$_5$), manganese oxide (MnO$_2$), and molybdenum oxide (MoO$_3$), due to their high

theoretical capacitances originated from the multivalent redox centers [19–23]. Nevertheless, the aforementioned materials suffer from sluggish ion/electron transportation because of their highly crystalized structure with anisotropic characteristics and wide bandgaps. In addition, the distinct volume expansion during charge-discharge (ion deintercalation-intercalation) results in rapid performance decay. Therefore, the exploration of advanced electrode materials with efficient charge storage capability is highly required.

As a typical transitional metal oxide, MoO$_3$ possess high theoretical specific capacitance due to the multielectron transfer process during proton intercalation-deintercalation [24, 25]. Compared with crystalline counterparts, nanosized amorphous MoO$_3$ (A-MoO$_3$) are highly desired for their disordered structures, good chemical stability, high elasticity, low internal energy, and large surface area, enabling isotropic

ion-diffusion, enhanced electrochemical dynamics, excellent mechanical robustness, and superior structure stability during charge/discharge cycling [26]. Ideally, the synthesis of A-MoO$_3$ should be convenient with tunable compositions (e.g., oxygen vacancies and hybridization), free of contamination (e.g., surfactants) for eliminating possible blockage of active sites, and scalable for industrial production. However, the currently utilized bottom-up strategies, for example, solvothermal reaction [27, 28], electrochemical deposition [26], and photochemical deposition [29], are subjected to numerous issues, including (i) special attention needs be paid to reaction environment (e.g., temperature) to stabilize the metastable amorphous phase, (ii) nonuniform coating resulted from unevenly distributed electric field on electrode surface, (iii) rigorous experimental conditions, e.g., ultraviolet illumination, (iv) possible contamination from organic additives, and (v) complicated procedures which are not suitable for massive preparation. Moreover, these methods are incompatible with the state-of-the-art fiber-spinning techniques [30, 31].

Herein, for the first time, high-performance fiber electrodes embedded with nanosized A-MoO$_{3-x}$ featuring an average particle diameter of 20 nm and rich oxygen vacancies are obtained *via* a newly developed top-down strategy by directly phase transformation of α-MoO$_3$ crystals. The underlying mechanism for amorphization and nanocrystallization is highlighted and attributed to the strengthened Jahn-Teller distortion in MoO$_6$ octahedra arising from the doubly degenerate ground state of Mo^{5+}. The enlarged interfacial contact between A-MoO$_{3-x}$ and rGO endues the obtained A-MoO$_{3-x}$/rGO hybrid fiber an ultrahigh C_V of 921.5 F cm^{-3} under 0.3 A cm^{-3} in 1 M H$_2$SO$_4$, enabling the assembled solid-state FSC superior C_V and E_V of 107.0 F cm^{-3} and 9.51 mWh cm^{-3}, respectively, together with outstanding flexibility, cyclic stability, and rate capability.

2. Results

When the degenerate orbitals in transition metal-based octahedral complexes are occupied by an odd number of electrons, the Jahn-Teller effect occurs through crystal distortion in order to lower the overall energy. Herein, the Jahn-Teller effect was employed for phase engineering of α-MoO$_3$ simply triggered by oxygen vacancies. α-MoO$_3$ belts with dimensional features in micron-scale (Figure S1) were synthesized *via* hydrothermal reaction between Mo powder and hydrogen peroxide at 220°C for 15.0 h. The as-synthesized MoO$_3$ possess well-defined belt-like morphology with a length of 5 to 30 μm and a width of 200 to 500 nm. The lattice spacings of ~0.36 nm and ~0.39 nm shown in Figure S2 are well indexed to (001) and (100) planes of α-MoO$_3$ [32]. The characteristic peaks in X-ray diffraction (XRD) pattern (Figure S3a) match those of α-MoO$_3$ crystals with orthorhombic phase well (JCPDs: 05-0508). In a typical experiment schematically illustrated in Figure 1(a), α-MoO$_3$ belts were hydrothermally reacted with graphene oxide (GO) nanosheets in sealed glass capillaries (~1 mm in diameter) at 160°C for 6.0 h to achieve nanosized

A-MoO$_{3-x}$ and simultaneously obtain A-MoO$_{3-x}$/rGO hybrid fibers. As indicated in Figure 1(b), the resultant A-MoO$_{3-x}$/rGO hybrid fiber possesses a wrinkle surface with a diameter of ~30.1 μm. Although no observable particles can be found under the cross-section view of A-MoO$_{3-x}$/rGO hybrid fiber (Figure 1(c)), C, O, and Mo are actually distributed uniformly, which was evidenced by the energy dispersive spectrometer (EDS). The fiber length was facilely adjusted by the size of a microreactor, and the obtained long A-MoO$_{3-x}$/rGO hybrid fiber (Figure 1(d)) could be bent and wound on a PTFE rod, demonstrating its good flexibility. The resultant A-MoO$_3$ nanoparticles (~20 nm in diameter) are evenly anchored on rGO nanosheets (Figure 1(e)), and the amorphous phase is formed with very small crystalline domains inside not completely transformed (Figures 1(f)–1(h)). The closed diffraction rings with several highlight points in the FFT pattern (Figure 1(h)) also suggest the existence of polycrystalline structure in the nanoparticles. This is in good accordance with the XRD pattern (Figure S3b), in which the characteristic peaks of α-MoO$_3$ crystals disappear after hydrothermal treatment and the broadened peak is attributable to rGO. By contrast, the characteristic XRD pattern of the orthonormal phase maintains when α-MoO$_3$ belts were hydrothermally treated without any additives or with graphite powder (Figure S4), indicating that GO is crucial for the amorphization and collapse of α-MoO$_3$ crystals.

Ex situ TEM images clearly reflect the morphology evolution of α-MoO$_3$ belts during hydrothermal reaction with GO from 0.5 to 10.0 h (Figure 2(a)), where the pristine α-MoO$_3$ belts with large size were collapsed into small particles at 0.5 h and fully converted to nanosized A-MoO$_{3-x}$ at 6.0 h. The size and phase transformation of α-MoO$_3$ belts can also be evidenced from the SEM images and XRD patterns of intermediate state A-MoO$_{3-x}$/rGO hybrid fibers (Figures S5 and S6). Furthermore, the chemical states and valance evolution of C and Mo were investigated by X-ray photoelectron spectroscopy (XPS). The four deconvoluted peaks of C 1s can be well ascribed to C-C (284.6 eV), C-OH (285.2 eV), C-O (286.9 eV), and O=C-OH (288.5 eV) on GO nanosheets, respectively, suggesting the existence of abundant oxygen-containing groups (Figure 2(b)). As expected, upon hydrothermal treatment, the oxygen-containing groups were effectively eliminated from GO nanosheets, restoring the high electrical conductivity. The controllable manipulation of the concentration of oxygen vacancies is observed from the fine-scanned Mo 3d region. The characteristic peaks at 232.9 eV (Mo^{6+} 3d$_{5/2}$) and 236.1 eV (Mo^{6+} 3d$_{3/2}$) tend to downshift (Figure 2(c)), suggesting that oxygen vacancies are gradually generated with an increasing content of Mo^{5+} (16.1 at%, 21.6 at%, 24.7 at%, and 63.4 at% at 0.5 h, 4.0 h, 6.0 h, and 10.0 h, respectively) and α-MoO$_3$ crystals are reduced under hydrothermal condition. The reaction process can be simplified as follows:

$$\text{MoO}_3 \xrightarrow{-\text{C-OH}} \text{Mo}_{1-x}^{6+}\text{Mo}_x^{5+}\text{O}_{3-x} \qquad (1)$$

The overall amorphization and collapse of α-MoO$_3$ belts can be ascribed to the strengthened Jahn-Teller
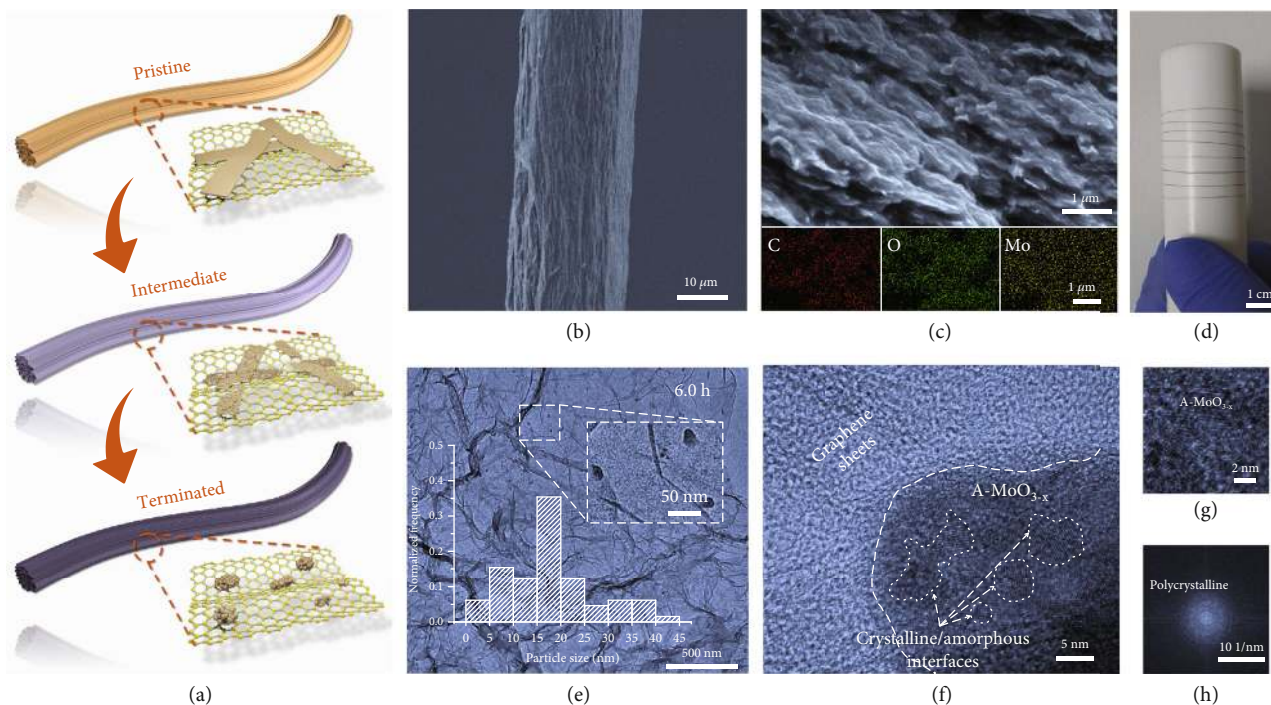
FIGURE 1: Synthesis and characterization of A-MoO$_{3-x}$/rGO hybrid fiber. (a) Schematic illustration showing the structure evolution of α-MoO$_3$ belts during the preparation of A-MoO$_{3-x}$/rGO hybrid fibers. (b) SEM (scanning electron microscope) image of A-MoO$_{3-x}$/rGO hybrid fiber obtained at 6.0 h. (c) Cross-sectional SEM image of the obtained A-MoO$_{3-x}$/rGO hybrid fiber and the corresponding EDS mapping. (d) Digital photograph of A-MoO$_{3-x}$/rGO hybrid fiber wounded on a PTFE rod. (e) TEM (transmission electron microscope) image of A-MoO$_{3-x}$/rGO hybrid fiber at the synthetic time of 6.0 h. The insets are particle size distribution of A-MoO$_{3-x}$ on rGO nanosheets and the local TEM image with higher magnification, respectively. (f–h) HRTEM and the corresponding FFT images of A-MoO$_{3-x}$/rGO hybrid fiber obtained at 6.0 h.

distortion, as illustrated in Figure 2(d). According to crystal field stabilization energy of α-MoO$_3$, lattice distortion happens in [MoO$_6$] unit due to the destroyed symmetry of electron cloud, which is known as the Jahn-Teller effect [33, 34]. In addition, the electronic instability of Mo^{5+}, which can be created by introducing oxygen vacancies in α-MoO$_3$, will further enhance the Jahn-Teller distortion, leading to changes in crystal and electronic structure [21, 35]. The formation of oxygen vacancies and the deformation of surface lattice were theoretically unveiled using density functional theory (DFT), giving further evidence on the strengthened Jahn-Teller distortion. As shown in Figure 3(a), surface oxygen atoms can be classified into three types, Ot, Oa, and Os, respectively, upon the differences of the chemical state (chemical bonding or van der Waals force). For example, Ot vacancy (V(Ot)) reserves the instinct lattice symmetry with slight atomic displacement, whereas V(Os) and V(Oa) induce large lattice deformation (Figure 3(b)), e.g., 6% of lattice shrink for V(Oa) [36, 37]. Since the oxygen-containing groups, e.g., C–OH, C=O, and -COOH, generally play a critical role in interface reactions, by taking GO nanosheets into consideration, approximate models of CH$_3$OH and H$_2$CO were adopted to elucidate the formation of oxygen vacancies. Our calculation shows that α-MoO$_3$ has a strong affinity towards C-OH groups rather than C=O, and the energy barrier for the linkage between Mo atom and -OH is 0.25 eV (Figure 3(c)). Based on Bader charge analysis, Oa and Os are more negatively charged than

Ot; consequently, H atoms are prone to contact with Oa and Os, forming an intermediate of *Oa-H (or Os-H) with an energy barrier of 0.55 eV. Subsequently, when a second protonation process occurs on the surface, an oxygen vacancy is generated together with a corresponding Mo^{5+} Jahn-Teller center, which would destabilize the octahedral environments via stretching and contraction Mo-O bonds and boost more Oa and Os site exploration [38–40]. Therefore, in our experiment, the abundant oxygen-containing functional groups (e.g., C-OH, C=O, and C-O-C as shown in Figure 2(b)) on GO nanosheets hydrothermally reacted with α-MoO$_3$ at 160°C. The accumulation of oxygen vacancies led to the rupture of Mo-O bonds in MoO$_6$ octahedra and the deformation of surface lattice. Ultimately, the amorphization and collapse of α-MoO$_3$ into amorphous nanoparticles were achieved.

Guided by the above mechanism, the electrochemical performance of the A-MoO$_{3-x}$/rGO fiber electrode was optimized via simply regulating the time of hydrothermal treatment and feeding ratio of GO and α-MoO$_3$. The cyclic voltammograms (CVs) at the scan rate of 2 mV s^{-1} were measured in a three-electrode configuration within the potential window between 0 and 0.8 V using Ag/AgCl (saturated KCl) as the reference electrode and H$_2$SO$_4$ (1 M) as the acidic electrolyte, respectively. As expected, moderate amount of oxygen vacancies, uniform loading of amorphous nanoparticles, and the mild reduction of GO nanosheets together endow the resultant A-MoO$_{3-x}$/rGO fiber the maximum
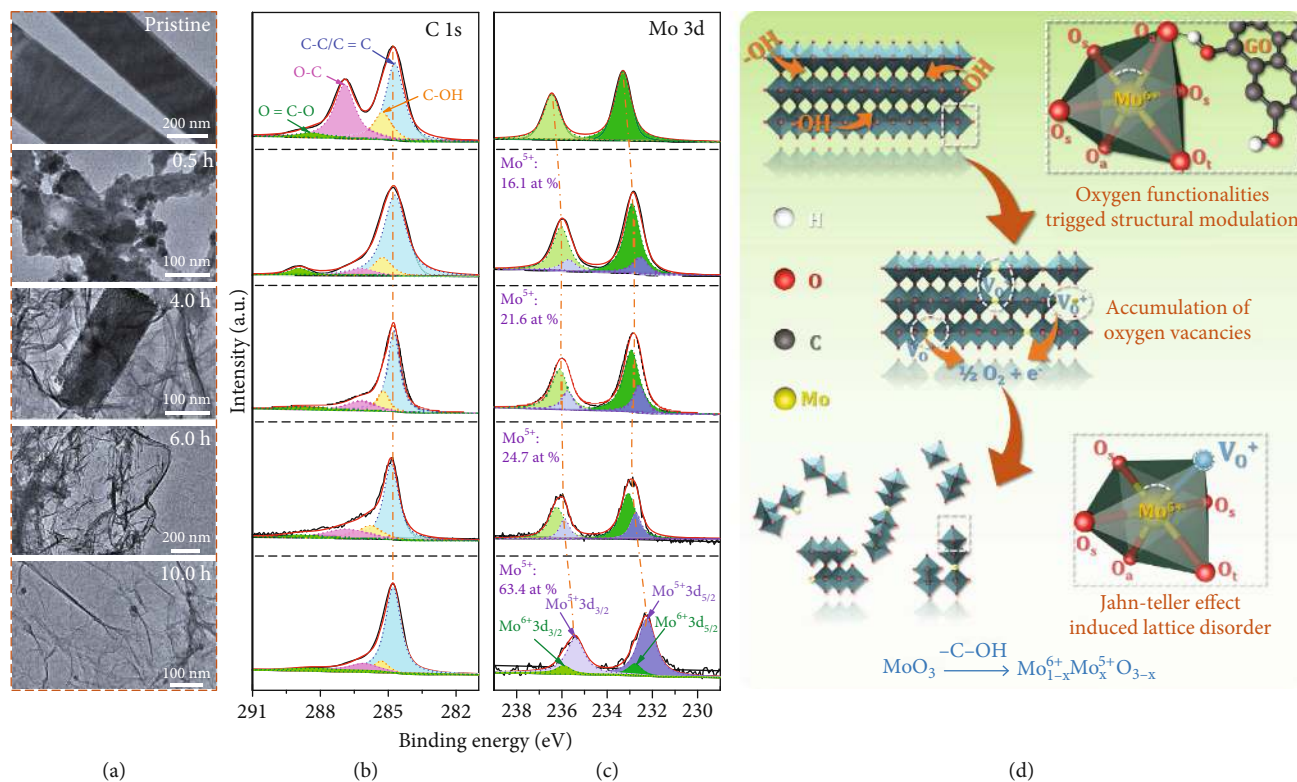
FIGURE 2: Structure evolution of α-MoO$_3$ belts during hydrothermal treatment. (a) TEM images of α-MoO$_3$ belts and A-MoO$_{3-x}$/rGO hybrid fibers obtained at different synthetic time. XPS spectra of (b) C 1s and (c) Mo 3d in pristine GO, bare α-MoO$_3$ belts, and hybrid fibers (A-MoO$_{3-x}$/rGO) obtained at different synthetic time. (d) The Jahn-Teller distortion during the reaction between α-MoO$_3$ and oxygen functionalities on GO.

current density in CV curves at 2 mV s^{-1} and longest discharge time in GCD (galvanostatic charge-discharge) profiles at 1.4 A cm^{-3} (Figure S7), respectively. The C_V calculated from GCD results measured at 1.4 A cm^{-3} peaks at 612.7 F cm^{-3} (corresponding to 1.33 F cm^{-2} at 3.1 mA cm^{-2}) for A-MoO$_{3-x}$/rGO fiber obtained at 6.0 h hydrothermal reaction with the feeding ratio of 2 : 1 between GO and α-MoO$_3$ (Figure 4(a)). It is noteworthy that the extended hydrothermal reaction time (10.0 h) leads to degradation of fiber performance for the feeding ratio of 4 : 1 and 2 : 1 probably attributable to the extensive elimination of the oxygen-containing groups on GO nanosheets, whereas the continuous capacitance increase for 1 : 1 samples can be ascribed to the incomplete conversion of α-MoO$_3$. This observation adheres to the above-proposed mechanism in Figure 2(d). Compared to the approximate rectangular-shaped CV curve of bare rGO fiber, the A-MoO$_{3-x}$/rGO fiber electrode exhibits much larger current density with three pairs of stable and prominent redox peaks which can be ascribed to the multielectron transfer process of the Mo centers (Figure 4(b)) [41]. By contrast, pristine α-MoO$_3$ belts show rapid capacitance decay during cycling (Figure S8). The optimized A-MoO$_{3-x}$/rGO fiber electrode delivered an ultrahigh C_V of 921.5 F cm^{-3} at 0.3 A cm^{-3}, retaining 397.8 F cm^{-3} at 7.0 A cm^{-3} (Figures 4(c) and S9). This performance is 2.5-fold improvement compared to that of bare rGO electrode and much superior to those of PANI/MWCNT

film (238 F cm^{-3}) [42], MoO$_{3-x}$ nanopaper (652 F cm^{-3}) [43], H$_x$MoO$_{3-y}$ (350 F cm^{-3}) [44], MoS$_2$/HGO fiber (448 F cm^{-3}) [45], and MoS$_2$-rGO fiber (491.1 F cm^{-3}) [46] reported in literatures (Figure 4(d)). The electrochemical behavior of A-MoO$_{3-x}$/rGO fiber electrode was further characterized using electrochemical impedance spectroscopy (EIS). The EIS slope of hybrid fiber electrode at low-frequency range is slightly lower than that of bare rGO fiber electrode, indicating compromised ion diffusion for hybrid fibers (Figure S10). In addition, by employing Dunn's approach [47, 48], the diffusion-contributed and capacitive-contributed capacitances of A-MoO$_{3-x}$/rGO hybrid fiber were calculated as illustrated in Figure S11. The result shows that at 2 mV s^{-1}, the hybrid fiber exhibits a C_V of ~732.0 F cm^{-3} with 50.6% capacitive contribution, attributable to the shortened ion diffusion pathway and improved electron transport conductivity of A-MoO$_{3-x}$ nanoparticles compared to α-MoO$_3$ crystals (Figure S12).

By, respectively, using A-MoO$_{3-x}$/rGO and rGO fibers as electrodes, symmetric FSCs were assembled. CV profiles in H$_2$SO$_4$/PVA gel electrolyte were obtained under 2 mV s^{-1}. The FSC based on rGO fiber exhibits an almost rectangular CV curve, indicating a typical EDLC behavior. Comparably, A-MoO$_{3-x}$/rGO FSC (Figure 5(a)) delivers a larger current density with a pair of obvious peaks corresponding to the redox chemistry on A-MoO$_{3-x}$. According to the GCD profiles in Figure 5(b), the A-MoO$_{3-x}$/rGO FSC exhibits an

(a)

(b)

(c)
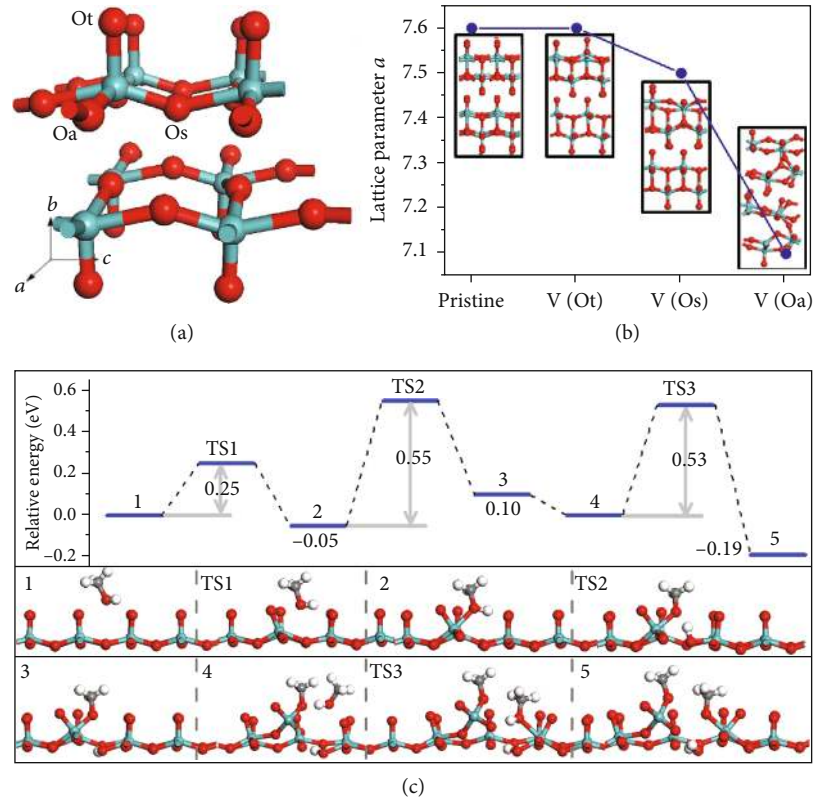
FIGURE 3: DFT calculation showing the lattice distortion of α-MoO$_3$. (a) Three types of surface oxygen atoms in α-MoO$_3$. (b) Dependence of lattice parameter change on the type of oxygen vacancy. (c) Reaction energy profile of vacancy formation (top) and the corresponding transition states and intermediates (bottom).

ultrahigh C_V of 107.0 F cm^{-3} (corresponding to 128.6 mF cm^{-2}, 3.94 mF cm^{-1}, and 78.3 F g^{-1}, respectively) at 0.14 A cm^{-3} (Figure 5(c)), which stands at a high level compared to that of other flexible supercapacitors, e.g., 10.9 F cm^{-3} for MnO$_2$-MWCNT fiber device (0.1 A cm^{-3}), 28.1 F cm^{-3} for Ni(OH)$_2$/CNT fiber device (0.4 A cm^{-3}), and 53.5 F cm^{-3} for MoO$_3$/rGO-based asymmetric device (0.1 A cm^{-3}) [49–51]. At 1.4 A cm^{-3}, the capacitance decreases to 55.3 F cm^{-3} with 51.7% retention. In contrast, only 26.9% of the initial capacitance (63.1 F cm^{-3}) was retained for the rGO-based device when the current density increased from 0.14 to 1.4 A cm^{-3}. According to the equations of $E_V = 1/2 \times C_V \times V^2$ and $P_V = E_V/t_{\text{discharge}}$ (E_V and P_V, respectively, represent the volumetric energy density and volumetric power density, V is the working voltage, while $t_{\text{discharge}}$ stands for the discharge time), E_V of the A-MoO$_{3-x}$/rGO FSC increases from 4.5 to 9.5 mWh cm^{-3} with the corresponding P_V varying between 0.84 and 0.06 W cm^{-3}. As shown in Figure 5(d), the performance of our device is superior to the flexible supercapacitors based on PPy/rGO/MWCNT (0.94 mWh cm^{-3}) [52], Fe$_2$O$_3$/PPy (0.22 mWh cm^{-3}) [53], FeOOH/PPy (2.0 mWh cm^{-3}) [54], CNT/N-rGO (6.3 mWh cm^{-3}) [55], and poly(styrene-butadiene-styrene)-G (6.6 mWh cm^{-3}) [56] and competitive to those based on G@PEDOT (7.0 mWh cm^{-3}) [57], PPy@nanocellulose (7.7 mWh cm^{-3}) [58], and PANI/rGO (8.8 mWh cm^{-3}) [59]. In addition, the A-MoO$_{3-x}$/rGO FSC exhibits excellent flexibility and cycling stability. 98.6% capacitance was sustained after

bending-unbending for 5000 cycles (Figure 5(e)), and 90.4% capacitance was retained after GCD cycling for 5000 times at 2.0 A cm^{-3} (Figure 5(f)).

To satisfy specific demands on energy and power, supercapacitors are required to be assembled in series or in parallel. Three hybrid fiber-based supercapacitors presenting similar CV and GCD behaviors were picked out. As shown in Figures 6(a) and 6(b), respectively, by connecting three devices in series, the output voltage can be extended to 3 times, while the connection in parallel tripled both the CV current and GCD discharge time. Moreover, as practical demonstration, a red LED array spelled word "IAM" could be lightened by a tandem system containing 6 FSCs on a piece of gauze (Figure 6(c)). Meanwhile, three hybrid fiber devices connected in series and braided on a cloth glove could also lighten a yellow LED. It is noteworthy that the yellow LED would neither extinguish nor diminish brightness with finger curved from 0° to 135°. These demonstrations indicate that the A-MoO$_{3-x}$/rGO hybrid fibers are promising to be applied in future wearable electronic devices to serve as main/emergency power supply as well as adapt to human daily movements.

3. Discussion

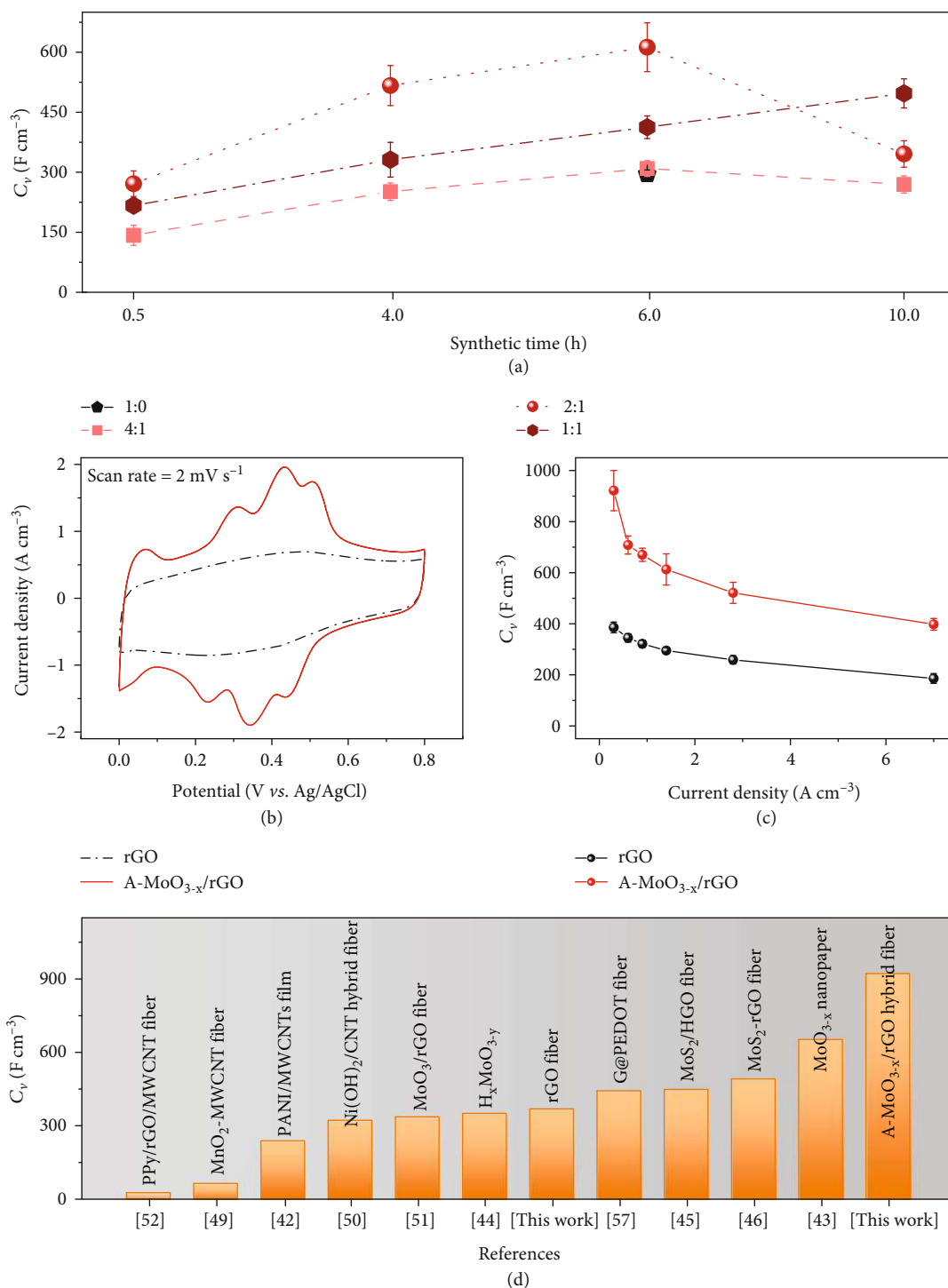In summary, the strengthened Jahn-Teller effect induced by the accumulation of Mo^{5+} was utilized for the phase

FIGURE 4: Electrochemical performances of A-MoO$_{3-x}$/rGO hybrid fiber electrodes. (a) C_V of A-MoO$_{3-x}$/rGO hybrid fiber electrodes versus synthetic time and the feeding ratio between GO and α-MoO$_3$ belts at 1.4 A cm^{-3}. (b) CV curves of hybrid fiber and rGO fiber at 2 mV s^{-1}. (c) Current density-dependent C_V of the hybrid fiber and rGO fiber. (d) Comparison of the highest C_V based on a single flexible electrode in this work and previous studies.

engineering of α-MoO$_3$ and A-MoO$_{3-x}$/rGO hybrid fiber electrode was successfully optimized *via* the controllable introduction of oxygen vacancies. In favor of amorphous MoO$_{3-x}$ nanoparticles with appropriate oxygen vacancy content evenly anchored on 3D interconnected graphene networks, the obtained hybrid fiber delivered an ultrahigh C_V of 921.5 F cm^{-3} together with outstanding cycling stability and flexibility, endowing the assembled FSC superior energy storage capability. The universality of the Jahn-Teller effect in crystal engineering other transitional metal oxide needs
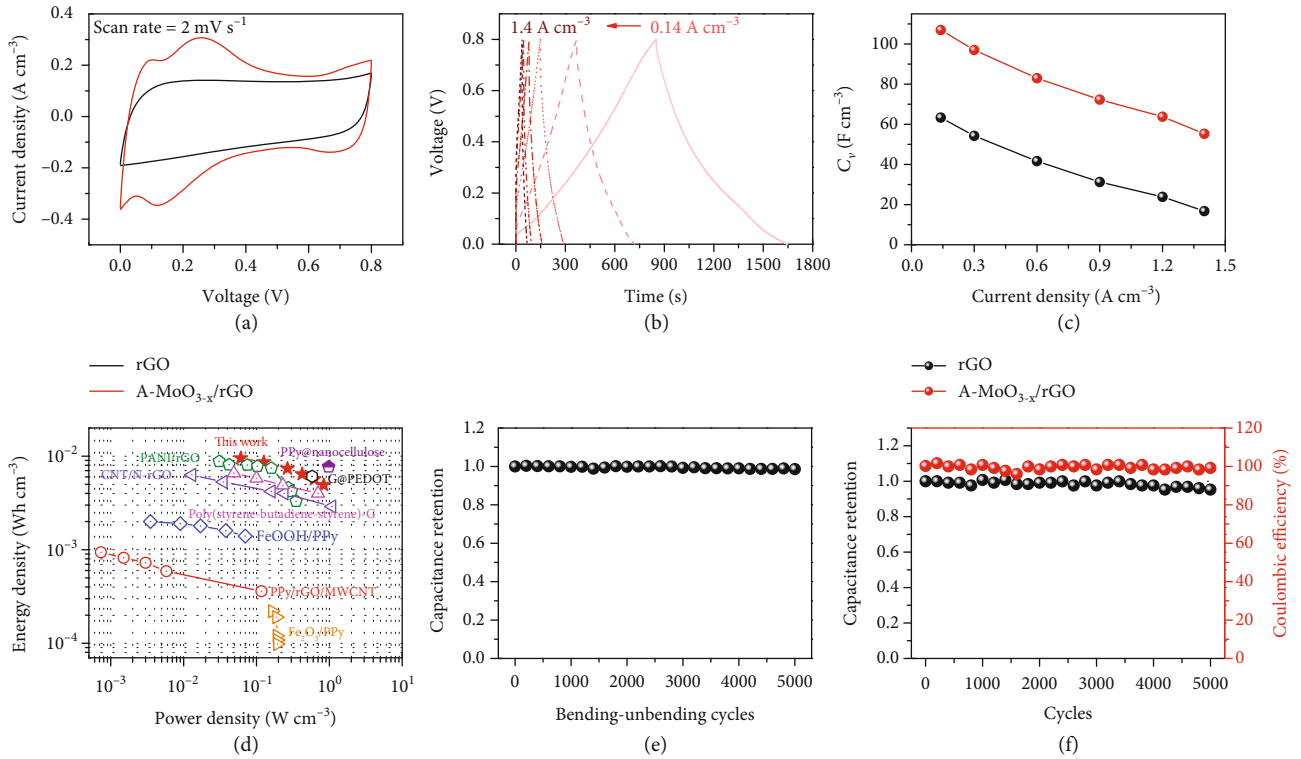
FIGURE 5: Electrochemical properties of assembled FSCs. (a) CV curves of flexible supercapacitors assembled by A-MoO$_{3-x}$/rGO hybrid fibers and bare rGO fibers at $2\,mV\,s^{-1}$. (b) GCD curves of FSC made of A-MoO$_{3-x}$/rGO hybrid fibers and bare rGO fibers. (c) C_V comparison of FSCs made of A-MoO$_{3-x}$/rGO hybrid fibers and bare rGO fibers, respectively. (d) Ragone plots of FSC made from A-MoO$_{3-x}$/rGO hybrid fibers compared with other flexible supercapacitors. (e) Bending-unbending and (f) cycling performance of FSC made of A-MoO$_{3-x}$/rGO hybrid fibers at $2.0\,A\,cm^{-3}$.

further investigation, which will be beneficial towards mass manufacturing high-performance hybrid fibers for future wearable energy storage systems.

4. Materials and Methods

4.1. Synthesis of GO Nanosheets. A modified Hummers' method was employed to synthesize GO nanosheets [60]. Briefly, expandable graphite flakes (1.0 g), NaNO$_3$ (0.5 g), and concentrated H$_2$SO$_4$ (46 mL) were mixed and placed in an ice bath under stirring. KMnO$_4$ (5.0 g) was slowly added to keep the reaction temperature below 20°C. Then, the mixture was heated to 35 ± 1°C and maintained for 8.0 h before adding deionized water (46 mL). 4 mL H$_2$O$_2$ (30 wt%) was subsequently added to the resultant suspension; then, GO nanosheets were collected and washed thoroughly.

4.2. Synthesis of α-MoO$_3$ Belts. Typically, 1.0 g Mo powder was firstly dissolved in 15 mL H$_2$O$_2$ (20 wt%) to obtain a light yellow solution. The mixture was hydrothermally heated at 220°C for 15.0 h, and the precipitate was collected.

4.3. Synthesis of A-MoO$_{3-x}$/rGO Hybrid Fibers. Typically, GO aqueous solution (4 mg mL^{-1}) was mixed with α-MoO$_3$ belts and the mass ratio was controlled $2:1$. After violently shaking, the mixture became homogeneous and subsequently was injected into a glass capillary with an inner diameter of ~1.0 mm. After being sealed at both ends using a welding

torch, the glass capillaries were heated in an electric oven at 160°C for 6.0 h. The obtained hydrogel fibers (self-assembled) were then thoroughly washed using deionized water and dried at 60°C in a vacuum oven.

4.4. Material Characterization. Field-emission scanning electron microscope (FESEM; JEOL, JSM-7800F) and transmission electron microscope (TEM; JEOL, 1400 PLUS) were employed for morphology characterizations. X-ray diffraction (XRD; smartlab; Cu Kα radiation, $\lambda = 1.5406$ Å) was used for identifying crystal structure. The confocal micro-Raman system (WITEC Alpha 300 M$^+$) was performed using a diode laser of 633 nm at ambient conditions. X-ray photoelectron spectroscopy (XPS) was carried out on a PHI Quantera spectrometer. Tensile tester (HY-0350) and Keithley 2400 were used for measuring the failure strength and electrical conductivity of fibers.

4.5. DFT Calculations. Vienna Ab initio Simulation Package (VASP) was adopted for theoretical calculations based on a gradient approximation described by Perdew-Burke-Ernzerhof (PBE) [61–63], ab initio molecular dynamics for open-shell transition metals, and ab initio molecular dynamics for open-shell transition metals. The wavefunctions in the core region were described by the projector augmented wave (PAW) method [64]. 10^{-5} eV and 0.02 eV Å^{-1} were, respectively, set for total energy and the Hellmann-Feynman force on each relaxed atom during geometry optimization. In order
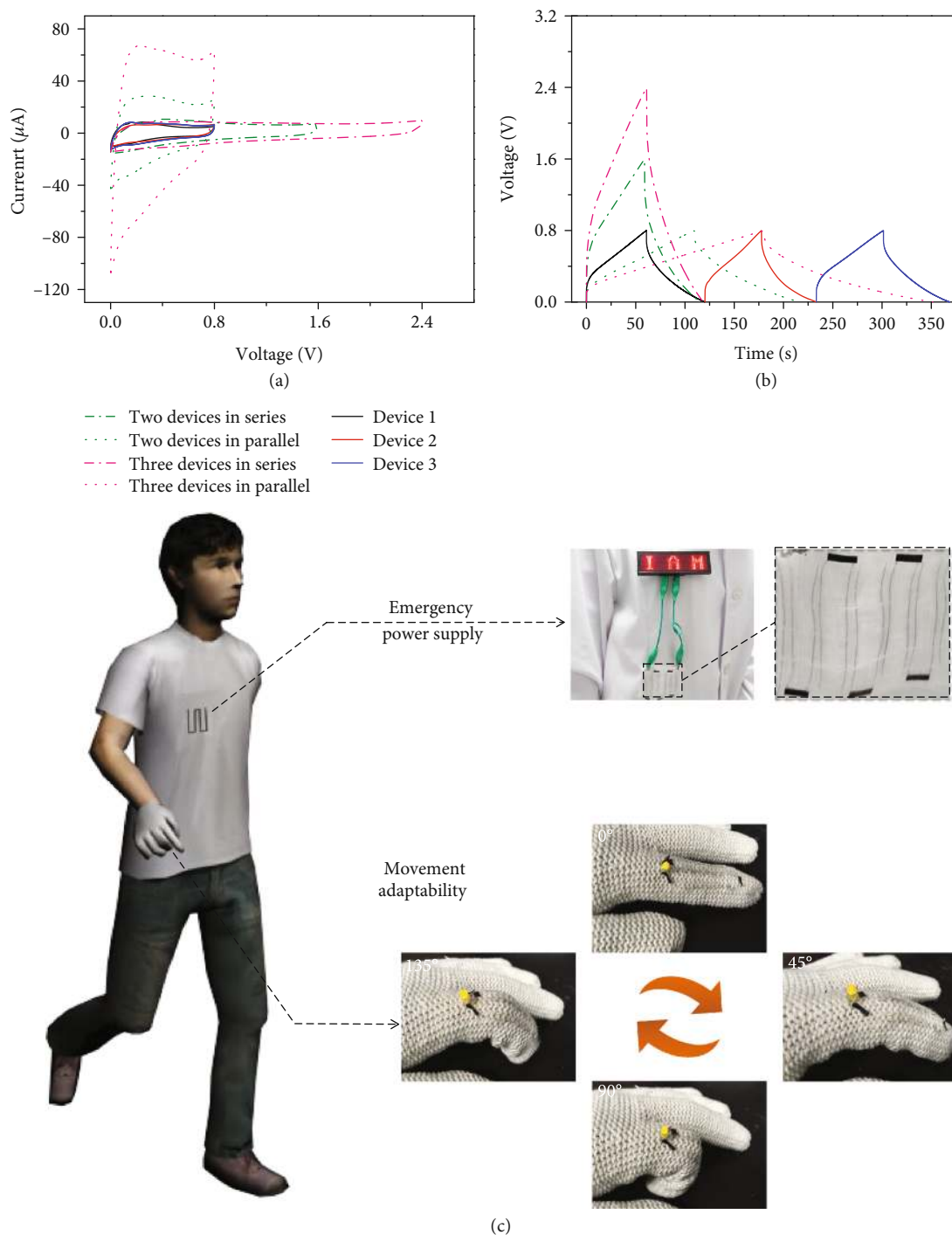
FIGURE 6: Practical demonstrations of FSCs made of A-MoO$_{3-x}$/rGO hybrid fibers. (a) CV curves at 5 mV s^{-1} and (b) GCD profiles at 0.9 A cm^{-3} of one, two, and three FSCs connected in series and in parallel. (c) Practical demonstration of flexible FSC tandems (containing 6 and 3 devices, respectively) for lightening LED pattern of "IAM" and a yellow LED mounted on a glove.

to exterminate any interaction, a spacing of 10 Å was chosen between two nanosheets. The activation barriers and transition states were determined by the climbing image nudged elastic band (NEB) method [65].

4.6. Electrochemical Measurement of Single Electrodes. The electrochemical performance of A-MoO$_{3-x}$/rGO hybrid fiber was tested in a three-electrode configuration with a reference electrode of Ag/AgCl (saturated KCl aqueous solution), a counter electrode of Pt plate, and the electrolyte of 1 M H$_2$SO$_4$. CV, and GCD measurements were performed on an electrochemical workstation (CHI660D, Chenhua). The fiber volume (V_{we}) was obtained according to $V_{we} = L \times \pi \times (D/2)^2$, where L represents fiber length while

D is fiber diameter. The electrochemical performance of pristine α-MoO$_3$ was also measured in the same three-electrode system.

4.7. Electrochemical Characterization of FSCs. Two ~1.5 cm long A-MoO$_{3-x}$/rGO hybrid fibers (diameter of ~50 μm) were placed closely on a polymeric (PET) substrate, on top of which H$_2$SO$_4$/PVA gel was coated. Ag paste was applied on one end of fiber electrode for better electrical connection. The electrochemical characterization and capacitance calculation of FSCs are similar to that of a single electrode.

Data Availability

The data used to support the findings of this study are included within the article and supplementary information files and/or may be requested from the authors.

Conflicts of Interest

The authors declare that there is no conflict of interest regarding the publication of this article.

Authors' Contributions

C.Y.Y. and G.Z.S. conceived the original concept. G.Z.S., Q.C., J.Y.Z., and W.H. supervised the study. C.Y.Y. and H.X. designed the experiments and prepared the materials. H.X. drew the schematic illustrations. C.Y.Y., R.Y.C., and Y.J.G. measured the electrochemical properties. C.Y.Y., Z.Y.H., X.Z., and Y.S. characterized the materials. W.X.J. did the DFT calculations. C.Y.Y., H.X., and G.Z.S. analyzed the data and wrote the manuscript. All authors commented on the manuscript revision. Chenyang Yu and Hai Xu contributed equally to this work.

Acknowledgments

Supplementary Materials

Figure S1: morphology characterization of α-MoO$_3$ belts. Figure S2: crystal interlayer spacing analysis of α-MoO$_3$ belts. Figure S3: crystal structure characterizations of α-MoO$_3$ belts and the obtained A-MoO$_{3-x}$/rGO hybrid fiber. Figure S4: crystal structure characterizations of hydrothermal treated α-MoO$_3$ belts with different conditions. Figure S5: morphology characterizations of A-MoO$_{3-x}$/rGO hybrid fibers obtained at different synthetic time. Figure S6: crystal structure characterizations of A-MoO$_{3-x}$/rGO hybrid fibers obtained at different synthetic time. Figure S7: electrochemical properties of A-MoO$_{3-x}$/rGO hybrid fibers obtained at different synthetic conditions. Figure S8: CV profiles of the pristine α-MoO$_3$ belts. Figure S9: electrochemical properties of the optimized A-MoO$_{3-x}$/rGO hybrid fiber. Figure S10: Nyquist plots of bare rGO fiber and A-MoO$_{3-x}$/rGO hybrid fibers, respectively. Figure S11: analysis of capacitance contribution of optimized A-MoO$_{3-x}$/rGO hybrid fiber. Figure S12: schematic illustration of the ion transport channels within α-MoO$_3$ crystals and A-MoO$_{3-x}$, respectively. *(Supplementary Materials)*

References

[1] D. J. Lipomi, M. Vosgueritchian, B. C. K. Tee et al., "Skin-like pressure and strain sensors based on transparent elastic films of carbon nanotubes," *Nature Nanotechnology*, vol. 6, no. 12, pp. 788–792, 2011.

[2] C. Pang, J. H. Koo, A. Nguyen et al., "Highly skin-conformal microhairy sensor for pulse signal amplification," *Advanced Materials*, vol. 27, no. 4, pp. 634–640, 2015.

[3] Y. Chen, J. Au, P. Kazlas, A. Ritenour, H. Gates, and M. McCreary, "Flexible active-matrix electronic ink display," *Nature*, vol. 423, no. 6936, p. 136, 2003.

[4] B. Comiskey, J. D. Albert, H. Yoshizawa, and J. Jacobson, "An electrophoretic ink for all-printed reflective electronic displays," *Nature*, vol. 394, no. 6690, pp. 253–255, 1998.

[5] G. Sun, J. Liu, L. Zheng, W. Huang, and H. Zhang, "Preparation of weavable, all-carbon fibers for non-volatile memory devices," *Angewandte Chemie, International Edition*, vol. 52, no. 50, pp. 13351–13355, 2013.

[6] G. Sun, X. Wang, and P. Chen, "Microfiber devices based on carbon materials," *Materials Today*, vol. 18, no. 4, pp. 215–226, 2015.

[7] D. Yu, Q. Qian, L. Wei et al., "Emergence of fiber supercapacitors," *Chemical Society Reviews*, vol. 44, no. 3, pp. 647–662, 2015.

[8] X. Chen, H. Lin, J. Deng et al., "Electrochromic fiber-shaped supercapacitors," *Advanced Materials*, vol. 26, no. 48, pp. 8126–8132, 2014.

[9] W. Gao, S. Emaminejad, H. Y. Y. Nyein et al., "Fully integrated wearable sensor arrays for multiplexed in situ perspiration analysis," *Nature*, vol. 529, no. 7587, pp. 509–514, 2016.

[10] Y. Liu, M. Pharr, and G. A. Salvatore, "Lab-on-skin: a review of flexible and stretchable electronics for wearable health monitoring," *ACS Nano*, vol. 11, no. 10, pp. 9614–9635, 2017.

[11] H. Sun, X. You, J. Deng et al., "Novel graphene/carbon nanotube composite fibers for efficient wire-shaped miniature energy devices," *Advanced Materials*, vol. 26, no. 18, pp. 2868–2873, 2014.

[12] Z. Zhang, X. Chen, P. Chen et al., "Integrated polymer solar cell and electrochemical supercapacitor in a flexible and stable fiber format," *Advanced Materials*, vol. 26, no. 3, pp. 466–470, 2014.

[13] H. Sun, Y. Zhang, J. Zhang, X. Sun, and H. Peng, "Energy harvesting and storage in 1D devices," *Nature Reviews Materials*, vol. 2, no. 6, article 17023, 2017.

[14] Y. Qin, X. Wang, and Z. L. Wang, "Microfibre-nanowire hybrid structure for energy scavenging," *Nature*, vol. 457, no. 7227, pp. 809–813, 2009.

[15] C. Yu, Y. Gong, R. Chen et al., "A solid–state fibriform super-capacitor boosted by host–guest hybridization between the carbon nanotube scaffold and MXene nanosheets," *Small*, vol. 14, no. 29, article 1801203, 2018.

[16] C. Yu, H. Xu, X. Zhao et al., "Scalable preparation of high performance fibrous electrodes with bio-inspired compact core–fluffy sheath structure for wearable supercapacitors," *Carbon*, vol. 157, pp. 106–112, 2020.

[17] J. Tang, R. R. Salunkhe, H. Zhang et al., "Bimetallic metal-organic frameworks for controlled catalytic graphitization of nanoporous carbons," *Scientific Reports*, vol. 6, no. 1, article 30295, 2016.

[18] Y. Li, J. Henzie, T. Park et al., "Fabrication of flexible microsu-percapacitors with binder-free ZIF-8 derived carbon films via electrophoretic deposition," *Bulletin of the Chemical Society of Japan*, vol. 93, no. 1, pp. 176–181, 2019.

[19] N. Yu, H. Yin, W. Zhang, Y. Liu, Z. Tang, and M. Q. Zhu, "High-performance fiber-shaped all-solid-state asymmetric supercapacitors based on ultrathin MnO_2 nanosheet/carbon fiber cathodes for wearable electronics," *Advanced Energy Materials*, vol. 6, no. 2, article 1501458, 2015.

[20] L. Hua, Z. Ma, P. Shi et al., "Ultrathin and large-sized vanadium oxide nanosheets mildly prepared at room temperature for high performance fiber-based supercapacitors," *Journal of Materials Chemistry A*, vol. 5, no. 6, pp. 2483–2487, 2017.

[21] I. A. de Castro, R. S. Datta, J. Z. Ou et al., "Molybdenum oxides-from fundamentals to functionality," *Advanced Materials*, vol. 29, no. 40, article 1701619, 2017.

[22] N. L. Wulan Septiani, Y. V. Kaneti, K. B. Fathoni et al., "Self-assembly of nickel phosphate-based nanotubes into two-dimensional crumpled sheet-like architectures for high-performance asymmetric supercapacitors," *Nano Energy*, vol. 67, article 104270, 2020.

[23] S. Makino, Y. Yamauchi, and W. Sugimoto, "Synthesis of electro-deposited ordered mesoporous RuO_x using lyotropic liquid crystal and application toward micro-supercapacitors," *Journal of Power Sources*, vol. 227, pp. 153–160, 2013.

[24] X. Wang, Y. Xie, K. Tang, C. Wang, and C. Yan, "Redox chemistry of molybdenum trioxide for ultrafast hydrogen-ion storage," *Angewandte Chemie, International Edition*, vol. 57, no. 36, pp. 11569–11573, 2018.

[25] X. Hu, W. Zhang, X. Liu, Y. Mei, and Y. Huang, "Nanostructured Mo-based electrode materials for electrochemical energy storage," *Chemical Society Reviews*, vol. 44, no. 8, pp. 2376–2404, 2015.

[26] S. Q. Wang, X. Cai, Y. Song, X. Sun, and X. X. Liu, "VOx@-MoO3Nanorod composite for high-performance supercapacitors," *Advanced Functional Materials*, vol. 28, no. 37, article 1803901, 2018.

[27] A. Michailovski, J. D. Grunwaldt, A. Baiker, R. Kiebach, W. Bensch, and G. R. Patzke, "Studying the solvothermal formation of MoO_3 fibers by complementary in situ EXAF-S/EDXRD techniques," *Angewandte Chemie, International Edition*, vol. 44, no. 35, pp. 5643–5647, 2005.

[28] G. Wang, Y. Ji, L. Zhang, Y. Zhu, P. I. Gouma, and M. Dudley, "Synthesis of molybdenum oxide nanoplatelets during crystallization of the precursor gel from its hybrid nanocomposites," *Chemistry of Materials*, vol. 19, no. 5, pp. 979–981, 2007.

[29] G. E. Buono-Core, G. Cabello, A. H. Klahn et al., "Growth and characterization of molybdenum oxide thin films prepared by

[30] photochemical metal-organic deposition (PMOD)," *Polyhedron*, vol. 29, no. 6, pp. 1551–1554, 2010.

[30] C. Yu, J. An, R. Zhou et al., "Microstructure design of carbonaceous fibers: a promising strategy toward high-performance weaveable/wearable supercapacitors," *Small*, vol. 16, no. 25, article 2000653, 2020.

[31] C. Yu, J. An, Q. Chen et al., "Recent advances in design of flexible electrodes for miniaturized supercapacitors," *Small Methods*, vol. 4, no. 6, article 1900824, 2020.

[32] L. Cai, P. M. Rao, and X. Zheng, "Morphology-controlled flame synthesis of single, branched, and flower-like α-MoO_3 nanobelt arrays," *Nano Letters*, vol. 11, no. 2, pp. 872–877, 2011.

[33] E. M. Plotnikova, M. Daghofer, J. van den Brink, and K. Wohlfeld, "Jahn-Teller effect in systems with strong on-site spin-orbit coupling," *Physical Review Letters*, vol. 116, no. 10, article 106401, 2016.

[34] L. Bai, Y. Zhang, L. Zhang et al., "Jahn-Teller distortions in molybdenum oxides: an achievement in exploring high rate supercapacitor applications and robust photocatalytic potential," *Nano Energy*, vol. 53, pp. 982–992, 2018.

[35] M. Okada, K. Ono, S. Yoshio, H. Fukuyama, and K. Adachi, "Oxygen vacancies and pseudo Jahn-Teller destabilization in cesium-doped hexagonal tungsten bronzes," *Journal of the American Ceramic Society*, vol. 102, no. 9, pp. 5386–5400, 2019.

[36] V. B. Sulimov, P. V. Sushko, A. H. Edwards, A. L. Shluger, and A. M. Stoneham, "Asymmetry and long-range character of lattice deformation by neutral oxygen vacancy in α-quartz," *Physical Review B*, vol. 66, no. 2, article 024108, 2002.

[37] K. Inzani, T. Grande, F. Vullum-Bruer, and S. M. Selbach, "A van der Waals density functional study of MoO_3 and its oxygen vacancies," *Journal of Physical Chemistry C*, vol. 120, no. 16, pp. 8959–8968, 2016.

[38] Z. H. Zhang, S. Y. Wu, B. T. Song, and X. F. Hu, "Investigations on the spin Hamiltonian parameters and defect structure for the interstitial Mo^{5+} centre in TiO_2," *Optik*, vol. 125, no. 18, pp. 5221–5224, 2014.

[39] W. C. Zheng, Y. Mei, and W. Q. Yang, "Defect model and spin-Hamiltonian parameters for the tetragonal Mo^{5+} and W^{5+} centers in Cs_2ZrCl_6 and Cs_2HfCl_6 crystals," *Philosophical Magazine*, vol. 89, no. 20, pp. 1621–1628, 2009.

[40] Y. Mei and W. C. Zheng, "Spin-Hamiltonian parameters and defect structure for the tetragonal Mo^{5+} center in the reduced $BaTiO_3$:Mo crystal," *Journal of Magnetism and Magnetic Materials*, vol. 348, pp. 51–54, 2013.

[41] K. Zhou, W. Zhou, X. Liu et al., "Ultrathin MoO_3 nanocrystalsself-assembled on graphene nanosheets via oxygen bonding as supercapacitor electrodes of high capacitance and long cycle life," *Nano Energy*, vol. 12, pp. 510–520, 2015.

[42] M. N. Hyder, S. W. Lee, F. Ç. Cebeci, D. J. Schmidt, Y. Shao-Horn, and P. T. Hammond, "Layer-by-layer assembled polyaniline nanofiber/multiwall carbon nanotube thin film electrodes for high-power and high-energy storage applications," *ACS Nano*, vol. 5, no. 11, pp. 8552–8561, 2011.

[43] L. Huang, B. Yao, J. Sun et al., "Highly conductive and flexible molybdenum oxide nanopaper for high volumetric supercapacitor electrode," *Journal of Materials Chemistry A*, vol. 5, no. 6, pp. 2897–2903, 2017.

[44] L. Huang, X. Gao, Q. Dong et al., "HxMoO3−ynanobelts with sea water as electrolyte for high-performance pseudocapacitors

and desalination devices," *Journal of Materials Chemistry A*, vol. 3, no. 33, pp. 17217–17223, 2015.

[45] C. Wang, S. Zhai, Z. Yuan et al., "A core-sheath holey graphene/graphite composite fiber intercalated with MoS_2 nanosheets for high-performance fiber supercapacitors," *Electrochimica Acta*, vol. 305, pp. 493–501, 2019.

[46] C. Yu, H. Xu, Y. Sun et al., "The incorporation of expanded 1T-enriched MoS_2 boosts hybrid fiber improved charge storage capability," *Carbon*, vol. 170, pp. 543–549, 2020.

[47] F. Zhang, T. Liu, M. Li et al., "Multiscale pore network boosts capacitance of carbon electrodes for ultrafast charging," *Nano Letters*, vol. 17, no. 5, pp. 3097–3104, 2017.

[48] H. S. Kim, J. B. Cook, H. Lin et al., "Oxygen vacancies enhance pseudocapacitive charge storage properties of MoO_{3-x}," *Nature Materials*, vol. 16, no. 4, pp. 454–460, 2017.

[49] P. Shi, L. Li, L. Hua et al., "Design of amorphous manganese oxide@multiwalled carbon nanotube fiber for robust solid-state supercapacitor," *ACS Nano*, vol. 11, no. 1, pp. 444–452, 2017.

[50] P. Shi, R. Chen, L. Li et al., "Holey nickel hydroxide nanosheets for wearable solid-state fiber-supercapacitors," *Nanoscale*, vol. 10, no. 12, pp. 5442–5448, 2018.

[51] W. Ma, S. Chen, S. Yang et al., "Flexible all-solid-state asymmetric supercapacitor based on transition metal oxide nanorods/reduced graphene oxide hybrid fibers with high energy density," *Carbon*, vol. 113, pp. 151–158, 2017.

[52] S. Wang, N. Liu, J. Su et al., "Highly stretchable and self-healable supercapacitor with reduced graphene oxide based fiber springs," *ACS Nano*, vol. 11, no. 2, pp. 2066–2074, 2017.

[53] L. Wang, H. Yang, X. Liu et al., "Constructing hierarchical tectorum-like α-Fe_2O_3/PPy nanoarrays on carbon cloth for solid-state asymmetric supercapacitors," *Angewandte Chemie, International Edition*, vol. 56, no. 4, pp. 1105–1110, 2017.

[54] X. Gong, S. Li, and P. S. Lee, "A fiber asymmetric supercapacitor based on FeOOH/PPy on carbon fibers as an anode electrode with high volumetric energy density for wearable applications," *Nanoscale*, vol. 9, no. 30, pp. 10794–10801, 2017.

[55] D. Yu, K. Goh, H. Wang et al., "Scalable synthesis of hierarchically structured carbon nanotube-graphene fibres for capacitive energy storage," *Nature Nanotechnology*, vol. 9, no. 7, pp. 555–562, 2014.

[56] I. Marriam, X. Wang, M. Tebyetekerwa et al., "A bottom-up approach to design wearable and stretchable smart fibers with organic vapor sensing behaviors and energy storage properties," *Journal of Materials Chemistry A*, vol. 6, no. 28, pp. 13633–13643, 2018.

[57] S. Padmajan Sasikala, K. E. Lee, J. Lim et al., "Interface-confined high crystalline growth of semiconducting polymers at graphene fibers for high-performance wearable supercapacitors," *ACS Nano*, vol. 11, no. 9, pp. 9424–9434, 2017.

[58] Z. Wang, P. Tammela, P. Zhang, M. Strømme, and L. Nyholm, "High areal and volumetric capacity sustainable all-polymer paper-based supercapacitors," *Journal of Materials Chemistry A*, vol. 2, no. 39, pp. 16761–16769, 2014.

[59] P. Li, Z. Jin, L. Peng et al., "Stretchable all-gel-state fiber-shaped supercapacitors enabled by macromolecularly interconnected 3D graphene/nanostructured conductive polymer hydrogels," *Advanced Materials*, vol. 30, no. 18, article 1800124, 2018.

[60] L. Hua, P. Shi, L. Li et al., "General metal-ion mediated method for functionalization of graphene fiber," *ACS Applied Materials and Interfaces*, vol. 9, no. 42, pp. 37022–37030, 2017.

[61] G. Kresse and J. Hafner, "Ab initio molecular dynamics for open-shell transition metals," *Physical Review B*, vol. 48, no. 17, pp. 13115–13118, 1993.

[62] G. Kresse and J. Furthmüller, "Efficient iterative schemes for ab initio total-energy calculations using a plane-wave basis set," *Physical Review B*, vol. 54, no. 16, pp. 11169–11186, 1996.

[63] J. P. Perdew, K. Burke, and M. Ernzerhof, "Generalized gradient approximation made simple," *Physical Review Letters*, vol. 77, no. 18, pp. 3865–3868, 1996.

[64] D. Joubert, "From ultrasoft pseudopotentials to the projector augmented-wave method," *Physical Review B*, vol. 59, no. 3, pp. 1758–1775, 1999.

[65] S. Grimme, "Semiempirical GGA-type density functional constructed with a long-range dispersion correction," *Journal of Computational Chemistry*, vol. 27, no. 15, pp. 1787–1799, 2006.